# Electronic, adsorption, and hydration structures of water-contained Na-montmorillonite and Na-beidellite through the first-principles method combined with the classical solution theory

Satoshi Hagiwara [1,*] Yasunobu Ando [2] Yuta Goto [3] Susumu Shinoki,[3] and Minoru Otani [1,†]

[1]*Center for Computational Sciences, University of Tsukuba, 1-1-1, Tenno-dai, Tsukuba, Ibaraki 305-8577, Japan*

[2]*Research Center for Computational Design of Advanced Functional Materials (CD-FMat), National Institute of Advanced Industrial Science and Technology (AIST), 1-1-1 Umezono, Tsukuba, Ibaraki 305-8568, Japan*

[3]*Iwaki Laboratory, Kunimine Industries Co., Ltd., 23-5, Kuidesaku, Jobanshimofunao-machi, Iwakishi, Fukushima 972-8312, Japan*

(Received 13 December 2021; accepted 9 February 2022; published 28 February 2022)

We investigated the electronic and hydration structures of montmorillonite (MMT) and beidellite (BEI) using a first-principles method combined with classical solution theory. Both MMT and BEI belong to a family of clay minerals with a layered structure containing water molecules and cations in the interlayer. First, we optimized the number of accumulated water molecules in the interlayer space and found the present results to be in reasonable agreement with previous experiments. Next, we refined the positions of the cations to determine the most stable structure based on the adsorption energy of the clay layers. We found that the cations in the interlayer stably adsorb to the clay layers and the most stable adsorption site is the center of the six-membered ring. The hydration structure strongly depends on the cation adsorption structure based on the charge density distribution of the water. In contrast, the electronic state is weakly dependent on the adsorption structure because of its insulating electronic structure. Therefore, our results strongly suggest that the physical properties of MMT and BEI arise from changes in the hydration structure induced by cation adsorption/desorption.

DOI: 10.1103/PhysRevMaterials.6.025001

## I. INTRODUCTION

The structural and chemical properties of clay minerals, which are ubiquitous at or near the earth's surface, have led to the wide utilization of these minerals in traditional ceramics as well as in modern functional nanomaterials [1–5]. In particular, the unique properties of clay minerals enable these minerals to be used as natural nanosized particles in catalytic, electrochemical, and biological materials. In addition, clay minerals are of significant importance as a material for interpreting the global climate, early earth environment, and life evolution [4,6]. Therefore, clay minerals have attracted considerable attention from researchers in various fields.

Both montmorillonite (MMT) and beidellite (BEI) belong to the 2:1 type of smectite group of clay minerals [7]. Both MMT and BEI have a layered structure with two tetrahedral sheets ($T_h$) combined with an octahedral sheet ($O_h$) in which the apical oxygen atoms are shared. The clay layer has a negative charge because of isomorphic substitutions resulting from the replacement of the $Al^{3+}$ ($Si^{4+}$) ion located at the center of the $O_h$ ($T_h$) structure by $Mg^{2+}$ ($Al^{3+}$) ions. Positive ions, such as $Li^+$, $Na^+$, $K^+$, and $Ca^{2+}$, are located in the interlayer space and compensate for the negative charge of the clay layer. These clay minerals are easily hydrated and swelled by accumulating many water molecules in the interlayer, which is a typical feature of MMT and BEI [8–10]. The swelling properties were observed as changes in the length of the $c$ axis of clays as a function of the mass ratio of $H_2O$ molecules to the dry clay $m_w/m_c$. The experimental results indicated that a range of one- to three-layered hydration shells is formed in the interlayer space of clay layers [11,12]. Therefore, insight into the interaction between clay and intercalated water molecules is important for understanding the physical properties of clay minerals.

Theoretically, atomic-scale simulation is a powerful tool for revealing the detailed interactions between solids and liquids. In this regard, classical molecular dynamics (MD)-based simulations have been used as a flexible method to study the swelling process of clay minerals [13–17]. In addition to classical mechanics, first-principles MD (FPMD) simulation is a more reliable method to investigate a solid-liquid interaction system [18–21]. However, the FPMD approach incurs huge computational costs because many sampling trajectories are necessary to describe the thermally averaged properties of the solution system. In addition, there are many configurations of interlayer cation types and isomorphic substituted atoms in smectites, and these parameters play a role for determining the properties of clay minerals. Therefore, a high-throughput theoretical method would be indispensable to conduct exhaustive studies on the detailed interactions between clays and water and the material properties of the clays.

In this paper, we used a method based on the flexible three-dimensional reference interaction site model (3D-RISM) [22] to probe the interactions between the clays and intercalated water in detail. In this paper, we used a $Na^+$ ion as the intercalated cation in MMT and BEI and termed these structures Na-MMT and Na-BEI, which are typical smectite structures. This paper is organized as follows: In Sec. II, we describe

*hagiwara@ccs.tsukuba.ac.jp
†otani@ccs.tsukuba.ac.jp

 

the 3D-RISM method, models of MMT and BEI, and provide computational details. Next, Sec. III presents the results and a discussion of the water content analysis, $Na^+$ adsorption energies and structures, and hydration structures. Then, the electronic structures of MMT and BEI are discussed based on the results of the charge distributions and density of states (DOS). Finally, we summarize the paper in Sec. IV.

## II. METHODS, COMPUTATIONAL MODELS, AND DETAILS

In this section, we first briefly describe the 3D-RISM method. Then we present the structural models of MMT and BEI. Lastly, the computational details are described.

### A. Methods

Here, we briefly explain the 3D-RISM method used in this paper. 3D-RISM is a hybrid solvation model [23–26], *that is*, the system of interest is treated as explicit particles by density functional theory (DFT) [27,28], and the particles in the liquid system are implicitly represented by RISM [29,30], which is the classical solution theory. In 3D-RISM, the total energy functional of the entire system is described by the Helmholtz free energy $A$ instead of the total energy of the DFT, $E_{\mathrm{DFT}}$, as follows:

$$A = E_{\mathrm{DFT}} + \Delta\mu_{\mathrm{solv}}. \tag{1}$$

Here, $\Delta\mu_{\mathrm{solv}}$ is the excess chemical potential obtained by the RISM solution. In 3D-RISM, $\Delta\mu_{\mathrm{solv}}$ is determined by the direct and total correlation functions [$c(\boldsymbol{r})$ and $h(\boldsymbol{r})$]. There are several formulations for $\Delta\mu_{\mathrm{solv}}$ at temperature $T$, and here we show the well-known Kovalenko-Hirata (KH) model as a representative [22]:

$$\Delta\mu_{\mathrm{solv}} = k_{\mathrm{B}}T\rho^{\mathrm{V}}\sum_{\gamma}\int d\boldsymbol{r}\left[\frac{1}{2}\left\{h_{\gamma}^{\mathrm{UV}}(\boldsymbol{r})\right\}^2\Theta\left(-h_{\gamma}^{\mathrm{UV}}(\boldsymbol{r})\right) - c_{\gamma}^{\mathrm{UV}}(\boldsymbol{r}) - \frac{1}{2}h_{\gamma}^{\mathrm{UV}}(\boldsymbol{r})c_{\gamma}^{\mathrm{UV}}(\boldsymbol{r})\right]. \tag{2}$$

Here U and V mean the explicit system (solute) and implicit solution (solvent), respectively, and $\gamma$ indicates RISM sites. $k_{\mathrm{B}}$ and $\Theta$ are Boltzmann constant and Heaviside step function, respectively. The 3D-RISM includes the interaction between the electronic and solution systems by simultaneously solving the Khon-Sham and 3D-RISM equations. Thus, the charge distributions of the classical solution perturb the quantum electronic system via the electrostatic potential, and the explicit system acts on the solution through van der Waals (vdW) and electrostatic potentials. In addition, 3D-RISM is formulated under the canonical condition; thus, the number of RISM particles in the unit cell is fixed. Therefore, we can determine the number of intercalated water molecules in the interlayer between the clay layers by searching for the lowest hydration energy.

### B. Computational models

Here we describe the computational models of the clay used in this paper. The typical chemical formula of Na-MMT (BEI) is $Na_xAl_{2-x}Mg_xSi_4O_{10}(OH)_2 \cdot nH_2O$ [$Na_xAl_2Si_{4-x}Al_xO_{10}(OH)_2 \cdot nH_2O$] [7,33]. Here, $x$ denotes the concentration of isomorphic substituted ions and intercalated cations, where the ideal value of $x$ is equal to 0.33 for MMT and BEI, and $n$ indicates the number of intercalated water molecules per unit formula. In this study, we treat the intercalated water molecules as an implicit system, and the clay layers and cations were represented as an explicit system. To understand the effect of $x$ on the physical properties of clay minerals, we used three different values, $x = 0.2$, 0.33, and 0.5, to construct models of the smectites. Figure 1 shows models of the supercell of the explicit system for Na-MMT (left) and Na-BEI (right) with $x = 0.33$ as a representative concentration. Here, we show the lattice parameters and basic structures based on the results of x-ray powder patterns [33]. As the basic structure of clay minerals, we assumed that the $Na^+$ ions are located at the center of the interlayer space between the clay layers. Henceforth, the structure of this interlayer is abbreviated as INT. The sizes of the supercell for MMT and BEI with $x = 0.2$, 0.33, and 0.5 are $5 \times 1 \times 1$, $3 \times 1 \times 1$, and $2 \times 1 \times 1$, respectively. As seen in Fig. 1, the clay layers of MMT and BEI comprise two tetrahedral sheets ($T_h$) and an octahedral sheet ($O_h$). We assigned the labels $T_h^U$ and $T_h^L$ to the upper and lower sheets $T_h$, respectively. Notably, we positioned the OH group at $O_h$ of the clay layers, as was the case in previous FPMD calculations [18,19,21]. For the BEI model, we assumed that one Si atom in $T_h^U$ and $T_h^L$ is isomorphically substituted by an Al atom; hence, we did not consider the electric polarization of the BEI layer throughout this paper.

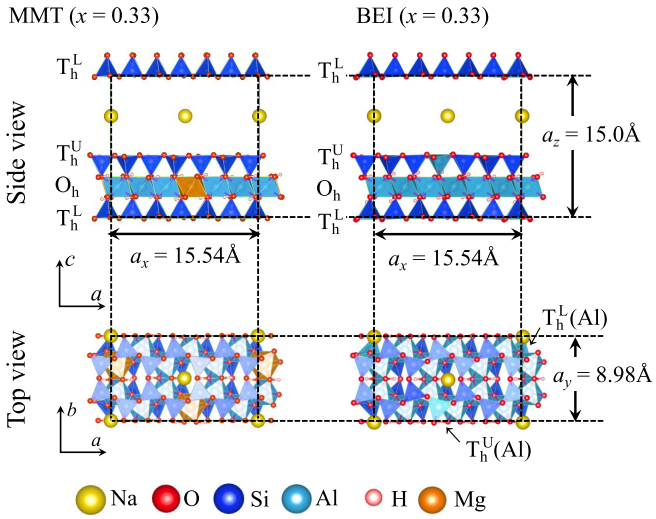


FIG. 1. Top and side views of the Na-MMT and Na-BEI models with $x = 0.33$ that were used in this paper. The pink, red, yellow, orange, cyan, and blue spheres represent H, O, Na, Mg, Al, and Si atoms, respectively. In this paper, the crystal structures are visualized using the VESTA program [31,32].

### C. Computational details

All calculations were carried out using QUANTUM ESPRESSO [34,35]. We used plane-wave basis sets within the ultrasoft pseudopotential framework [36–38]. The cutoff energies for the wave functions and augmented charge were

set to 40 Ry and 320 Ry, respectively, and the pseudopotential data with nonlinear core correction [39] were taken from the Garrity, Bennett, Rabe, and Vanderbilt (GBRV) table [40]. We prepared the supercell models of MMT and BEI with three different values of $x$: $x = 0.20$, 0.33, and 0.50. The converged $\boldsymbol{k}$-point samplings depended on the sizes of the supercells. The sizes $1 \times 3 \times 1$, $2 \times 3 \times 1$, and $3 \times 3 \times 1$ were adopted for $x = 0.20$, 0.33, and 0.50, respectively. According to a previous study, the vdW correction for the exchange-correlation functional plays a significant role in reproducing clay mineral structures [41–43]. Therefore, we employed the spin-unpolarized vdW-type exchange-correlation functional developed by Hamada [44]. In this paper, the number of $Na^+$ ions in the unit cell was fixed at two for MMT and BEI, and the isomorphically substituted ionic sites for each concentration were determined as the lowest formation energy $E_F$ using a conventional DFT calculation. The results of $E_F$ and optimized lattice parameters for MMT and BEI can be found in the Appendix. Note that we optimized lattice parameters only for $a$- and $b$-axis directions while fixing the lattice parameter in the $c$ axis to the result of the powder x-ray diffraction [33].

In the 3D-RISM calculations, the cutoff energy for the correlation functions was 240 Ry and the temperature parameter of the RISM solution was set to 300 K. We used a modified simple point charge model [45] for the implicit water molecules and the Clay-FF type force field [46] was employed as the nonbonding Lennard-Jones parameters for the explicit particles. The iterative calculation for determining the correlation functions was accelerated by the modified direct inversion of the iterative subspace method [47], of which the criteria for the root mean square of the residual for the total correlation function was $1.0 \times 10^{-5}$. We adopted the KH type of closure function [48] to close the RISM equations, and the hydration free energy was also determined by the charging formula of the KH model shown as Eq. (2).

## III. RESULTS AND DISCUSSIONS

In this section, we discuss the results we obtained for the hydration-free energies, the number of intercalated water molecules, adsorption energies, and structures of $Na^+$ ions for MMT and BEI. This is followed by a discussion of the dependence of the differences in the hydration structures on the adsorption structures. Then, we present the results of the charge distributions in the clay layers and $Na^+$ ions with $Na^+$ adsorption structures. Finally, the electronic structures of the clays were explained by the DOS.

### A. Hydration free energies and number of intercalated water molecules

Figure 2(a) shows the results of the hydration free energies $\Delta G_{hyd}$ as a function of the total number of intercalated water molecules $N_W$ in the unit cells per unit area $S$. Here, the calculations of $\Delta G_{hyd}$ were performed using the INT structure with fixed atomic positions. Previously, Ando *et al.* showed that the intercalated water affects the stable adsorption site of the cations in a layered material [49]. Therefore, we first determine the number of intercalated waters without $Na^+$ ion adsorption.

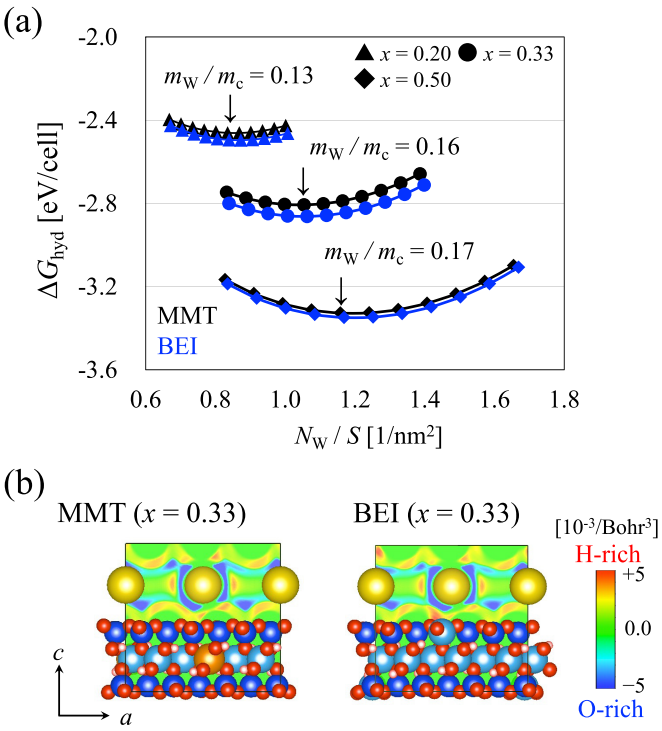


FIG. 2. (a) The hydration free energies $\Delta G_{hyd}$ for each $x$ as a function of the number of water molecules $N_W$ per unit area $S$. (b) Contour map of the charge density distributions of the water for MMT (left) and BEI (right) with $x = 0.33$. The downward arrows denote the lowest values of $\Delta G_{hyd}$, and $m_w/m_c$ obtained by the optimized $N_W$ are also provided. The black and blue symbols denote MMT and BEI, respectively.

All $\Delta G_{hyd}$ curves as a function of $N_W/S$ show the convex downward curvatures, which is consistent with previous 3D-RISM calculations [50–52]. This feature arises from forming a void in the water and the screening effect on the electrostatic interactions between the solute and solvent. The former and latter effects are related to the instability and stability of the solute, respectively. When $N_W/S$ is relatively small, the formation of a void in water is easy, and the screening effect of waters on the clays is relatively weak. By increasing $N_W/S$, the clays become unstable due to the increase in the void formation energy. In contrast, the increased screening effect of waters makes the clays more stable. Therefore, by competition of these effects, the $\Delta G_{hyd}$ curve becomes the convex-downward function with increasing $N_W/S$.

The values of $\Delta G_{hyd}$ were determined to be negative, and $\Delta G_{hyd} < 0$ indicates that water intercalation is thermodynamically favorable for the formation of clay minerals. Therefore, intercalated water molecules play an important role in the thermodynamic stability of smectites. The lowest value of $N_W/S$ is proportional to the value of $x$. This result is explained by the repulsive electrostatic interaction between $Na^+$ ions because a large $x$ denotes a dense concentration of $Na^+$ per unit area owing to the maintenance of charge neutrality of the system. Therefore, to lower the repulsive interaction, many $H_2O$ molecules accumulate in the interlayer of clays for which $x$ is large.

By employing the lowest $\Delta G_{\mathrm{hyd}}$, we can determine $m_{\mathrm{w}}/m_{\mathrm{c}}$ for MMT and BEI, and the results of $m_{\mathrm{w}}/m_{\mathrm{c}}$ are shown as downward arrows in Fig. 2, respectively. In previous studies, $m_{\mathrm{w}}/m_{\mathrm{c}}$ was estimated as a function of the $c$-axis length (or water vapor pressure) both experimentally [12,53] and theoretically [13,54,55]. For a $c$-axis length of 15 Å, the reported value of $m_{\mathrm{w}}/m_{\mathrm{c}}$ ranges from 0.16 to 0.20, which corresponds to two-layered hydration shells in the interlayer space. The present results for $m_{\mathrm{w}}/m_{\mathrm{c}}$ for $x = 0.3$ and 0.5 agree reasonably well with the experimental range. However, for $x = 0.2$, we discovered that $m_{\mathrm{w}}/m_{\mathrm{c}}$ was underestimated compared to the experimental value. This result is attributed to the relatively lower concentration of cation charges per unit area. Thus, the relatively low charge concentration of $Na^+$ leads to weak hydration, owing to the weakened electrostatic interaction between the cations and water molecules. According to previous studies [55,56], the results of $m_{\mathrm{w}}/m_{\mathrm{c}}$ by classical MD are either an underestimation or are in agreement with the lower bound of the experimental value of $m_{\mathrm{w}}/m_{\mathrm{c}}$, which is consistent with the present result. This difference in $m_{\mathrm{w}}/m_{\mathrm{c}}$ between the theory and experiment was interpreted to indicate water adsorption at other locations in the clays and/or the presence of interstratified phases [55,56]. Therefore, we consider the concentration of substituted ions to be related to the water retention of the clays and their mechanisms. Subsequent analyses were conducted using the optimized values of $N_{\mathrm{W}}$ for MMT and BEI.

Figure 2(b) shows the results of the charge density distributions of the water molecules for MMT and BEI at $x = 0.33$ without the $Na^+$ adsorption. We can clearly observe the formation of the hydration shells around the $Na^+$ ions, and the O and H atoms tend to be distributed around $Na^+$ and near $T_h$, respectively. This density distribution corresponds to a typical hydration structure of an outer-sphere complex, which is consistent with the previous results of the constrained FPMD [18,19,21]. Therefore, we consider 3D-RISM capable of reproducing the qualitative features of the hydration structure for MMT and BEI. For BEI, $T_h$ attracts the charge density of H atoms more than MMT. This result mainly arises from the difference in the location of the substituted ions between the clay types, as discussed above. Therefore, the $T_h$ value of BEI attracts more H atoms than MMT.

### B. Adsorption energies and structures of $Na^+$ ions

Here, we consider the adsorption structure of $Na^+$ on the clay layer. To determine the stable adsorption structure, we defined the adsorption energy $A_{\mathrm{ads}}$ of $Na^+$ in the MMT and BEI layers as follows:

$$A_{\mathrm{ads}} = -\{A(\mathrm{ads}) - A(\mathrm{INT})\}, \tag{3}$$

where $A$(ads) and $A$(INT) indicate the free energies of the adsorbed and INT structures, respectively. Here, we consider $T_h^U$ as the adsorption layer, and several adsorption sites are assumed. Figures 3(a) and 3(b) show the results of $A_{\mathrm{ads}}$ with a single $Na^+$ adsorption for MMT and BEI with $x = 0.33$, respectively. We also show the initially assumed adsorption sites of $Na^+$ around the center of a six-membered siloxane ring (hollow site). The results of $A_{\mathrm{ads}}$ are positive, which indicates that $Na^+$ tends to adsorb to $T_h^U$. Notably, for BEI, a

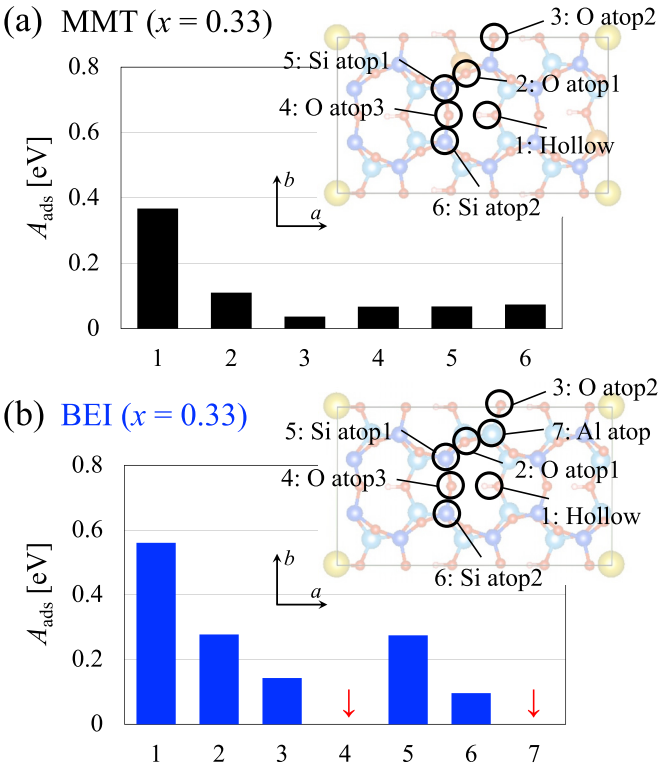


FIG. 3. Adsorption energies $A_{\mathrm{ads}}$ for a single $Na^+$ adsorbed onto (a) MMT and (b) BEI at $x = 0.33$. The initial adsorption sites for MMT and BEI assumed in this paper are also shown. For simplicity, we show only a $Na^+$ ion at the interlayer, $O_h$, and $T_h^U$ as the clay structures. The red downward arrows indicate unstable adsorption sites, and $Na^+$ moves toward the sites denoted hollow.

single $Na^+$ at the Si atop and O atop1 sites moved to the bridge site and we could not identify stable adsorption structures of $Na^+$ around the O atop2 and Al atop sites, as shown by the red downward arrows. The hollow site has the largest value of $A_{\mathrm{ads}}$ for both MMT and BEI, which indicates that the hollow site is the most stable adsorption site. The highest values of $A_{\mathrm{ads}}$ for MMT and BEI are 0.38 eV and 0.58 eV, respectively. The magnitudes of $A_{\mathrm{ads}}$ correspond to the typical energy of physisorption owing to the nonbonding interaction. Thus, the orbital hybridization between the adsorbate and clay layer is expected to be negligibly small, which is discussed later. In addition, in previous FPMD simulations, the interpretation of the adsorption site of $Na^+$ depends on the duration of the evolution. This result is attributed to the small adsorption energy of $Na^+$, as shown here, and the drawback of dynamical simulation methods. In contrast to the dynamical simulation, the 3D-RISM method provides thermally averaged hydration structures and $A_{\mathrm{ads}}$ by the one-shot calculation. This is one of the main advantages of our static simulation and allows the evaluation of an energetically stable structure.

Next, we discuss $A_{\mathrm{ads}}$ for the two $Na^+$ ions adsorbed to the MMT and BEI layers. Figure 4 shows the results of $A_{\mathrm{ads}}$ for the $Na^+$ adsorption as well as the adsorption structures. Here, we employed the hollow site as the most stable site for $Na^+$ adsorption and considered two configurations for the adsorption of two $Na^+$ ions: one $Na^+$ ion adsorbed to $T_h^U$

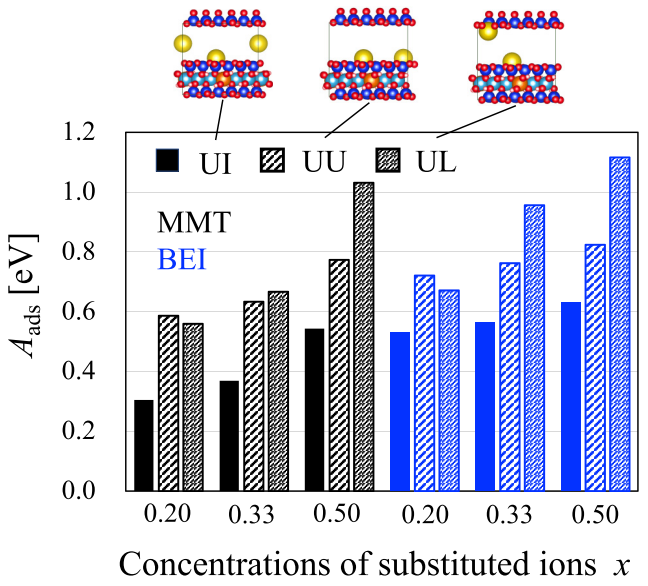


FIG. 4. Upper panels: Adsorption structures with one $Na^+$ ion (UI), two $Na^+$ ions adsorbed to $T_h^U$ and $T_h^L$ (UL), and two $Na^+$ ions adsorbed to $T_h^U$ (UU). Lower panel: Adsorption energies $A_{ads}$ for MMT and BEI at $x = 0.20$, $x = 0.33$, and $x = 0.50$. The filled, wide striped, and narrow striped bars denote $A_{ads}$ for the UI, UU, and UL structures, respectively. The black and blue bars indicate MMT and BEI, respectively.

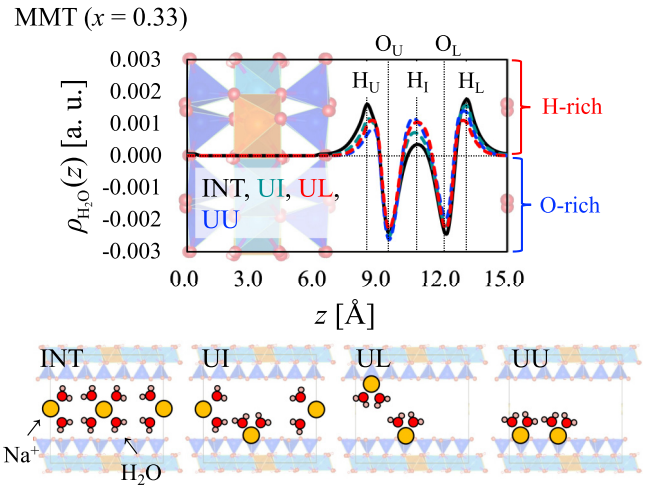


FIG. 5. Laterally averaged charge density distributions of the water $\rho_{H_2O}(z)$ for MMT with $x = 0.33$ (upper panel) and schematics of the hydration structure for the $Na^+$ ion with water molecules (lower panel). The black, green, red, and blue curves denote the INT, UI, UL, and UU structures, respectively. The yellow, red, and pink circles represent $Na^+$ ions, O atoms, and H atoms, respectively.

and the other $Na^+$ ion adsorbed to $T_h^L$, and both $Na^+$ ions adsorbed to $T_h^U$. Hereafter, the former and latter structures are abbreviated as UL and UU, respectively. Both $A_{ads}$(UL) and $A_{ads}$(UU) are higher than $A_{ads}$(UI); Hence, two $Na^+$ ions can adsorb to the clay layer, and the UL and UU structures are more stable than UI. In addition, we found that an increase in $x$ enhances the difference between $A_{ads}$(UL) and $A_{ads}$(UI). This result can be interpreted as an increase in the electrostatic interactions between the clay layer and $Na^+$ ions by increasing the concentration of the substituted ions.

We discuss the dependence of the stable adsorption structure on the value of $x$ for the two types of $Na^+$ adsorption. For $x \geqslant 0.33$, the UL structures are more stable than UU because $A_{ads}$(UL) is higher than $A_{ads}$(UU). Because the distance between the adsorbed $Na^+$ ions in the UL structure is sufficiently large compared to that for UU, the UL structure lowers the repulsive electrostatic interaction between the $Na^+$ cations. As a result of this, the UL structures are energetically favorable above $x = 0.33$. For $x = 0.20$, the tendency of $A_{ads}$ for the two types of $Na^+$ adsorption is opposite to that for $x \geqslant 0.33$. To understand the origin of this difference, we carried out conventional DFT calculations and obtained $A_{ads}$ without the hydration effect (not shown here). However, we did not find a qualitative difference in $A_{ads}$ with and without hydration effects. Therefore, the slightly larger $A_{ads}$ for the UU structure compared to that for UL is attributable to the difference in the electrostatic interactions between the adsorption structures. In addition, the $Na^+$ adsorption alters polarization vectors in the $c$-axis direction. Since the configuration of the polarization vector relates to structural stabilization, to determine a globally stable adsorption structure, we need to consider such macroscopic interaction for lower values of $x$.

Here, we mention an alternative approach for understanding the cation transfer mechanism in clay minerals. The properties of the cation transport from bulk water to the clay bulk also play a significant role in the applications of the clay minerals [21,57]. For approaching the cations at the MMT/water interface, we need to treat the chemical potential of implicit waters as constant because the inserting cations might push aside the waters in the clay minerals. To address this, the effective screening medium method combined with Laue-represented RISM (ESM-RISM) is one of the suitable methods, which is formulated under the grand canonical ensemble [50].

### C. Change in hydration structures after $Na^+$ adsorption

Here we discuss the hydration structures with and without $Na^+$ adsorption. After $Na^+$ adsorption on the clay layer, a rearrangement of interlayer water distributions occurs, which is evident from the results of the laterally averaged charge density of water $\rho_{H_2O}(z)$ shown in Fig. 5. Here, we depict $\rho_{H_2O}(z)$ for MMT with $x = 0.33$ as a representative, and the positive and negative values of $\rho_{H_2O}(z)$ are derived from the H and O atoms, respectively. Overall, $\rho_{H_2O}(z)$ is distributed only in the interlayer region, and $Na^+$ adsorption affects the charge density distribution of H atoms and does not alter the oxygen charge distribution. The adsorption of a single $Na^+$ ion causes the positive charges around $H_U$ and $H_I$ to decrease and increase, respectively. This change in $\rho_{H_2O}(z)$ originates from the H atoms of water directed toward $H_I$ to hydrate the adsorbed $Na^+$ ions. Therefore, as shown in the lower panels of Fig. 5, the interlayer side of the adsorbed $Na^+$ is hydrated, and this hydration structure corresponds to a typical inner-sphere complex structure (ISC). When the $Na^+$ configuration changes from UI to UL (or UU), $\rho_{H_2O}$ at $H_I$ increases because the hydration structure changes from OSC to ISC. Because $Na^+$ ions adsorb to $T_h^U$ and $T_h^L$ in the UL structure, $\rho_{H_2O}(z)$

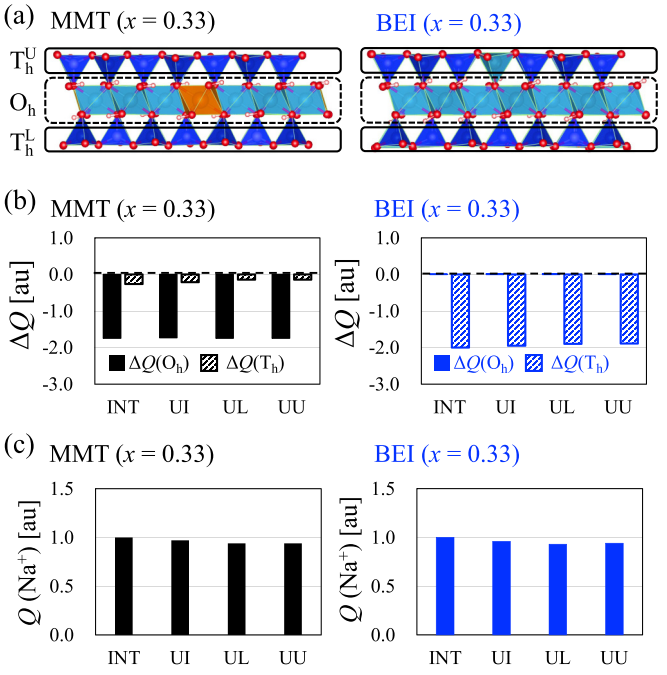


FIG. 6. Changes in Bader charges $\Delta Q$ of each layer and $Na^+$ ions for (a) MMT and (b) BEI at $x = 0.33$. (c) Definitions of sliced sheet regions used in the charge analysis for MMT and BEI. The black, green, and blue bars denote the $\Delta Q$ of the $Na^+$ ions and the outer and center layers, respectively. Here, $\Delta Q$ for the $Na^+$ ions is averaged by the number of $Na^+$ and for a single side of the outer layer.

is symmetrically distributed around $H_I$. In contrast, in the UU structure, $Na^+$ adsorption results in the generation of an electric field, which is screened by the distributed charge of the water molecules. Therefore, we conclude that the hydration structure is sensitive to changes in the configuration of the intercalated cations.

### D. Bader charge analysis and density of states

Here, we discuss the change in the charge distribution of MMT and BEI owing to $Na^+$ adsorption. First, a Bader charge analysis was carried out to determine the charge distribution partitioned by each atomic site [58–60]. In subsequent analyses, we divided the clay layer into upper and lower $T_h$ and $O_h$ regions, as shown in Fig. 6(a). Then, we integrated Bader charges ($Q$) for each atomic site in each clay layer. Figure 6(b) shows the results of the layer-by-layer charge states for MMT and BEI. The negative charges of each layer in MMT and BEI are distributed across $O_h$ and $T_h$, depending on the position of the isomorphous substituents. This result is the origin of the difference in the electrostatic interactions between MMT and BEI. In addition, we found the layer-by-layer charge distribution of MMT and BEI to be independent of the $Na^+$ adsorption. This result is also found in the averaged Bader charges of $Na^+$ ions $Q(Na^+)$, as shown in Fig. 6(c). We found a slight decrease in $Q(Na^+)$ with an increase in the number of adsorbed $Na^+$ ions. However, the extent to which $Q(Na^+)$ changed is negligible. This result implies that the orbital hybridization caused by the overlap in the wave

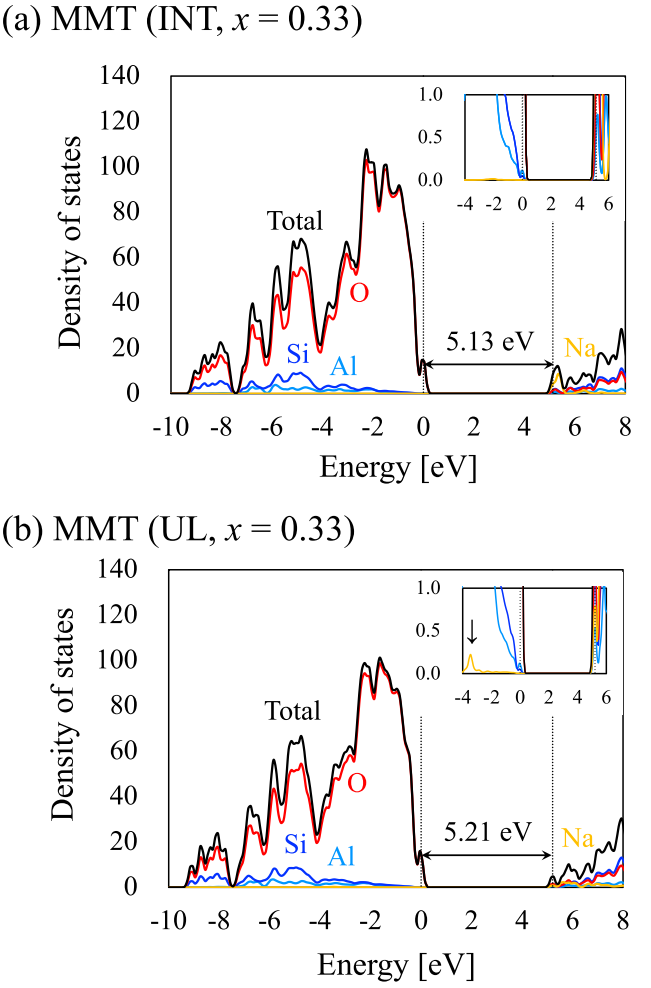


FIG. 7. Density of states (DOS) for MMT at $x = 0.33$ with (a) OSC and (b) UL structures. The horizontal axis denotes the energy measured from the valence band maximum (VBM). The black curve represents the total DOS, and the red, green, blue, and yellow curves represent the projected DOS for Al, Si, O, and Na, respectively. Insets: Enlarged views of total and projected DOS near VBM.

functions between cations and the clay layer is negligibly small. Therefore, we consider the electronic state of the clay mineral to be independent of the adsorption structure.

Finally, we discuss the dependence of the electronic structure of the clay on the $Na^+$ adsorption. Figure 7 shows the results of the total DOS and projected DOS. Here, we used the energy zero as the valence band maximum, and the results of INT for MMT ($x = 0.33$) and DOS for the UL structure are shown in Figs. 7(a) and 7(b), respectively. Note that the band gap is underestimated, a well-known drawback of local and semilocal density functionals [61,62]. The band gap of MMT is approximately 5 eV, which is consistent with that for dry MMT (4.6 eV) calculated in a previous first-principles study with a semilocal density functional [63]. Ferreira *et al.* has also reported the experimental band gap of 4.0 eV for the iron-doped dry MMT. The result of the band gap using DFT with the hybrid functional [64] well reproduces the experiment, and both the *d*-band state of doped iron and *p*-state of oxygen

locate around the valence band maximum and conduction band minimum. For quantitative discussion, we need to use the hybrid functional. As a consequence of $Na^+$ adsorption, the electronic state of Na appears near −3.5 eV shown as the inset in Fig. 7(b). However, the overall DOS structure is not altered significantly. Thus, this result of the DOS indicates the small orbital hybridization between the $Na^+$ ions and clay layers. Recently, Ando *et al.* analyzed the electronic structure of MXene with various surface terminations [49]. MXenes are also a family of clay-type materials with a layered structure and intercalated water molecules and cations. Because MXenes have metallic electronic structures, electrons in the valence band can be easily moved compared to Na-MMT and Na-BEI. Therefore, charge transfer between the cations and MXene layers is facilitated by adsorption of the cation to the MXene layer. From the above discussions, we concluded that the electronic structure of the clay is insensitive to the configuration of the interlayer cations because of its insulating nature.

## IV. SUMMARY

We investigated the fundamental physical properties of water containing Na-MMT and Na-BEI using the 3D-RISM method. The results of the mass ratio between the intercalated water and dry clays agreed reasonably well with those determined in the previous experiment. The difference in the mass ratio between the theoretical and experimental results is considered to exist as a result of water adsorption to the interface and surface of the clay particles. We computed the adsorption energy of $Na^+$ to clay layers for various adsorption sites and configurations. Based on the adsorption energy results, $Na^+$ ions can adsorb to the clay layers, and the stable adsorption site is referred to as the center of the six-membered ring. The hydration structure of the cations strongly depends on the $Na^+$ adsorption structures. On the other hand, the electronic structure of clays is insensitive to changes in the $Na^+$ configuration. According to the DOS analysis, this result can be understood as indicative of an insulating electronic structure. Therefore, we consider the main physical properties of Na-MMT and Na-BEI to depend on the hydration structures induced by $Na^+$ adsorption.

## ACKNOWLEDGMENTS

This paper was supported by MEXT as the Program for Promoting Research on the Supercomputer Fugaku (Fugaku Battery & Fuel Cell Project), Grant No. JPMXP1020200301. This paper was also partially supported by by Elements Strategy Initiative for Catalysts and Batteries (ESICB) of the Ministry of Education, Culture, Sports, Science and Technology (MEXT) (No. JPMXP0112101003). Parallel computations were performed using the supercomputer Fugaku provided by the RIKEN Center for Computational Science/FLOW provided by Nagoya University (Projects No. hp200131 and No. hp210173). We also used the computational resources of the supercomputer at the Institute for Solid State Physics at the University of Tokyo.

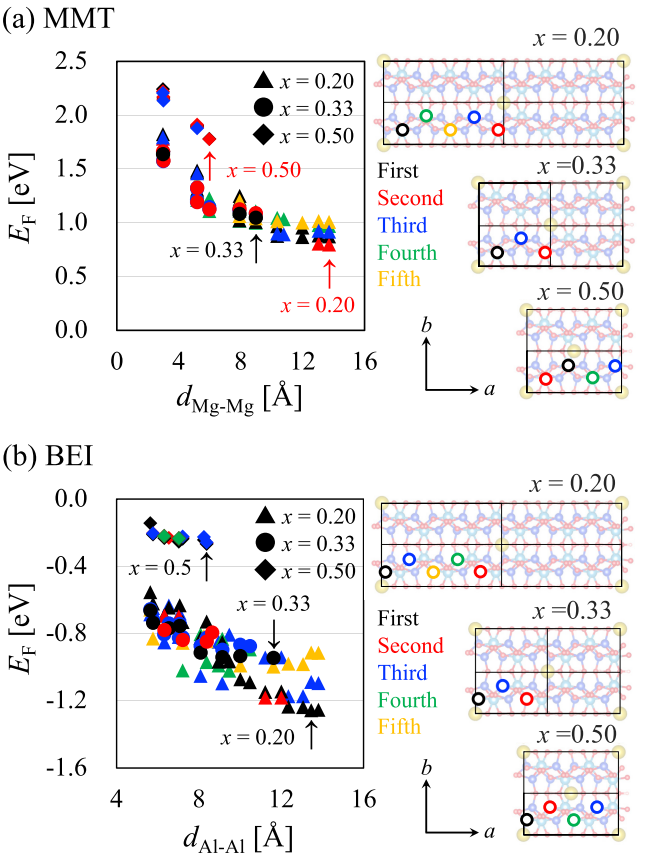


FIG. 8. Formation energies $E_F$ for (a) MMT and (b) BEI as a function of the distance between isomorphically substituted ions $d$. Filled triangles, circles, and diamonds indicate $x = 0.20$, 0.33, and 0.50, respectively. The arrows show the lowest $E_F$ for each $x$. We show the first choice of substituted ion sites (open circles) with the top view of the atomic arrays in the right panels. The black, red, blue, green, and yellow colors denote the first-, second-, third-, fourth-, and fifth nearest sites of $Na^+$ ions, respectively.

## APPENDIX: FORMATION ENERGIES AND LATTICE PARAMETERS

In this Appendix, we discuss the results of the formation energy and lattice constants in the lateral directions. First, we determined the isomorphic substitution ion sites for MMT and BEI as the minimum formation energies $E_F$. All analyses were performed using conventional DFT calculations with experimental lattice constants [33]. Figures 8(a) and 8(b) show the results of $E_F$ for MMT and BEI as a function of the distance between the substitution ions ($d_{Mg-Mg}$ or $d_{Al-Al}$), respectively. The color of the open circles indicates the order of the first substituted ion site measured from the nearest Na position. $E_F$ for MMT and BEI are defined as follows:

$$\begin{aligned} E_F(\mathrm{MMT}, x) = {} & 2/x[E(\mathrm{MMT}, x) \\ & - \{E(\mathrm{subs}) + xE(\mathrm{Na}) - xE(\mathrm{Al}) \\ & + x/2E(\mathrm{Mg})\}], \\ E_F(\mathrm{BEI}, x) = {} & 2/x[E(\mathrm{BEI}, x) \\ & - \{E(\mathrm{subs}) + xE(\mathrm{Na}) - x/2E(\mathrm{Si}) \end{aligned}$$

TABLE I. Optimized lattice constants in the $a$- and $b$-axis directions for MMT and BEI with $x = 0.20$, 0.33, and 0.50, as well as experimental data taken from Ref. [33]. Notably, the theoretical value is normalized by the size of the supercell repetitions.

| | MMT | | | BEI | | | |
|---|---|---|---|---|---|---|---|
| | 0.20 | 0.33 | 0.50 | 0.20 | 0.33 | 0.50 | Expt. |
| $a$ Å | 5.22 | 5.23 | 5.24 | 5.20 | 5.20 | 5.22 | 5.18 |
| $b$ Å | 9.01 | 9.02 | 9.05 | 8.99 | 8.99 | 9.01 | 8.98 |

$$+xE(\mathrm{Al})\}],$$

where $E(\mathrm{MMT}, x)$ [$E(\mathrm{BEI}, x)$] and $E(\mathrm{subs})$ represent the total energies for MMT (BEI) with and without isomorphous substitutions per unit formula, respectively. $E(\mathrm{Na})$, $E(\mathrm{Al})$, $E(\mathrm{Si})$, and $E(\mathrm{Mg})$ are the total energies of the Na, Al, Si, and Mg bulk crystals, respectively. Here, bcc, fcc, diamond, and hcp structures were employed for the Na, Al, Si, and Mg crystals, respectively. Overall, $E_{\mathrm{F}}$ decreases with increasing distance between the substituted ions, reducing the repulsive electrostatic interaction. Notably, although the results of $E_{\mathrm{F}}$ for MMT are generally positive, they become negative values when the hydration energy is taken into account.

After identifying the sites at which ion substitution takes place, we carried out cell optimization to obtain the optimized lattice parameters for MMT and BEI. For the lattice relaxation, we fixed the $Na^+$ positions and a lattice constant in the $c$-axis direction. Table I provides the results of the lattice constants along the $a$ and $b$ axes, which agree well with the experimental values. The results of the lattice constants were used for the 3D-RISM calculations throughout this paper.


[1] F. Bergaya and G. Lagaly, Dev. Clay Sci. **1**, 1 (2006).
[2] S. Dasgupta and B. Toeroek, Org. Prep. Proc. Int. **40**, 1 (2008).
[3] J. Herney-Ramirez, M. A. Vicente, and L. M. Madeira, Appl. Catal. B **98**, 10 (2010).
[4] C. H. Zhou and J. Keeling, App. Clay Sci. **74**, 3 (2013).
[5] L. Zhang, W.-B. Zhang, S.-S. Chai, X.-W. Han, Q. Zhang, X. Bao, Y.-W. Guo, X.-L. Zhang, X. Zhou, S.-B. Guo *et al.*, J. Electrochem. Soc. **168**, 070558 (2021).
[6] V. K. Pearson, M. A. Sephton, A. T. Kearsley, P. A. Bland, I. A. Franchi, and I. Gilmour, Meteorit. Planet. Sci. **37**, 1829 (2002).
[7] N. Güven, in *Smectites: Hydrous Phyllosilicates*, Reviews in Mineralogy, Vol. 19, edited by S. W. Bailey (Mineralogical Society of America, Cambridge University Press, 1988), p. 497–559.
[8] L. Aylmore and J. Quirk, Nature (London) **183**, 1752 (1959).
[9] P. F. Low and J. F. Margheim, Soil Sci. Soc. Am. J. **43**, 473 (1979).
[10] P. F. Low, Soil Sci. Soc. Am. J. **44**, 667 (1980).
[11] T. Sato, T. Watanabe, and R. Otsuka, Clays and Clay Minerals **40**, 103 (1992).
[12] M. Fu, Z. Zhang, and P. Low, Clays and Clay Minerals **38**, 485 (1990).
[13] S. Karaborni, B. Smit, W. Heidug, J. Urai, and E. Van Oort, Science **271**, 1102 (1996).
[14] L. Zhang, X. Lu, X. Liu, J. Zhou, and H. Zhou, J. Phys. Chem. C **118**, 29811 (2014).
[15] Y.-W. Hsiao and M. Hedström, J. Phys. Chem. C **121**, 26414 (2017).
[16] Y. Li, A. K. Narayanan Nair, A. Kadoura, Y. Yang, and S. Sun, Ind. Eng. Chem. Res. **58**, 1396 (2019).
[17] K. B. Thapa, K. S. Katti, and D. R. Katti, Langmuir **36**, 11742 (2020).
[18] T. Ikeda, S. Suzuki, and T. Yaita, J. Phys. Chem. A **119**, 8369 (2015).
[19] T. Ikeda, J. Chem. Phys. **145**, 124703 (2016).
[20] A. Seppälä, E. Puhakka, and M. Olin, Clay Minerals **51**, 197 (2016).
[21] M. Okumura, S. Kerisit, I. C. Bourg, L. N. Lammers, T. Ikeda, M. Sassi, K. M. Rosso, and M. Machida, J. Environ. Radioact. **189**, 135 (2018).
[22] A. Kovalenko and F. Hirata, J. Chem. Phys. **110**, 10095 (1999).
[23] V. Barone and M. Cossi, J. Phys. Chem. A **102**, 1995 (1998).
[24] A. Klamt, F. Eckert, and W. Arlt, Annu. Rev. Chem. Biomol. Eng. **1**, 101 (2010).
[25] R. Sundararaman and W. A. Goddard III, J. Chem. Phys. **142**, 064107 (2015).
[26] A. M. Maldonado, S. Hagiwara, T. H. Choi, F. Eckert, K. Schwarz, R. Sundararaman, M. Otani, and J. A. Keith, J. Phys. Chem. A **125**, 154 (2021).
[27] P. Hohenberg and W. Kohn, Phys. Rev. **136**, B864 (1964).
[28] W. Kohn and L. J. Sham, Phys. Rev. **140**, A1133 (1965).
[29] F. Hirata and P. J. Rossky, Chem. Phys. Lett. **83**, 329 (1981).
[30] F. Hirata, B. M. Pettitt, and P. J. Rossky, J. Chem. Phys. **77**, 509 (1982).
[31] K. Momma and F. Izumi, J. Appl. Crystallogr. **41**, 653 (2008).
[32] K. Momma and F. Izumi, J. Appl. Crystallogr. **44**, 1272 (2011).
[33] A. Viani, A. F. Gualtieri, and G. Artioli, Am. Mineral. **87**, 966 (2002).
[34] P. Giannozzi, S. Baroni, N. Bonini, M. Calandra, R. Car, C. Cavazzoni, D. Ceresoli, G. L. Chiarotti, M. Cococcioni, I. Dabo *et al.*, J. Phys.: Condens. Matter **21**, 395502 (2009).
[35] P. Giannozzi, O. Andreussi, T. Brumme, O. Bunau, M. B. Nardelli, M. Calandra, R. Car, C. Cavazzoni, D. Ceresoli, M. Cococcioni *et al.*, J. Phys.: Condens. Matter **29**, 465901 (2017).
[36] D. Vanderbilt, Phys. Rev. B **41**, 7892 (1990).
[37] K. Laasonen, R. Car, C. Lee, and D. Vanderbilt, Phys. Rev. B **43**, 6796 (1991).
[38] K. Laasonen, A. Pasquarello, R. Car, C. Lee, and D. Vanderbilt, Phys. Rev. B **47**, 10142 (1993).
[39] S. G. Louie, S. Froyen, and M. L. Cohen, Phys. Rev. B **26**, 1738 (1982).
[40] K. F. Garrity, J. W. Bennett, K. M. Rabe, and D. Vanderbilt, Comput. Mater. Sci. **81**, 446 (2014).
[41] V. K. Voora, W. Al-Saidi, and K. D. Jordan, J. Phys. Chem. A **115**, 9695 (2011).
[42] C. G. Fonseca, V. S. Vaiss, F. Wypych, R. Diniz, and A. A. Leitao, Appl. Clay Sci. **143**, 212 (2017).
[43] G. Ulian, D. Moro, and G. Valdrè, Minerals **11**, 501 (2021).
[44] I. Hamada, Phys. Rev. B **89**, 121103(R) (2014).

[45] H. J. C. Berendsen, J. P. M. Postma, W. F. von Gunstaren, and J. Hermans, in *Intermolecular Forces*, edited by B. Pullman (Reidel, Springer Netherlands, 1981), p. 331.
[46] R. T. Cygan, J.-J. Liang, and A. G. Kalinichev, J. Phys. Chem. B **108**, 1255 (2004).
[47] A. Kovalenko, S. Ten-no, and F. Hirata, J. Comput. Chem. **20**, 928 (1999).
[48] A. Kovalenko and F. Hirata, Chem. Phys. Lett. **290**, 237 (1998).
[49] Y. Ando, M. Okubo, A. Yamada, and M. Otani, Adv. Funct. Mater. **30**, 2000820 (2020).
[50] S. Nishihara and M. Otani, Phys. Rev. B **96**, 115429 (2017).
[51] A. Sugahara, Y. Ando, S. Kajiyama, K. Yazawa, K. Gotoh, M. Otani, M. Okubo, and A. Yamada, Nat. Commun. **10**, 850 (2019).
[52] K. Kim, Y. Ando, A. Sugahara, S. Ko, Y. Yamada, M. Otani, M. Okubo, and A. Yamada, Chem. Mater. **31**, 5190 (2019).
[53] R. Mooney, A. Keenan, and L. Wood, J. Am. Chem. Soc. **74**, 1371 (1952).
[54] E. Boek, P. Coveney, and N. Skipper, Langmuir **11**, 4629 (1995).
[55] E. J. Hensen and B. Smit, J. Phys. Chem. B **106**, 12664 (2002).
[56] J. Cases, I. Bérend, G. Besson, M. Francois, J. Uriot, F. Thomas, and J. Poirier, Langmuir **8**, 2730 (1992).
[57] T. Ohkubo, T. Okamoto, K. Kawamura, R. Guégan, K. Deguchi, S. Ohki, T. Shimizu, Y. Tachi, and Y. Iwadate, J. Phys. Chem. A **122**, 9326 (2018).
[58] E. Sanville, S. D. Kenny, R. Smith, and G. Henkelman, J. Comput. Chem. **28**, 899 (2007).
[59] W. Tang, E. Sanville, and G. Henkelman, J. Phys.: Condens. Matter **21**, 084204 (2009).
[60] M. Yu and D. R. Trinkle, J. Chem. Phys. **134**, 064111 (2011).
[61] A. Seidl, A. Görling, P. Vogl, J. A. Majewski, and M. Levy, Phys. Rev. B **53**, 3764 (1996).
[62] C. Hu, R. Ogura, N. Onoda, S. Konabe, and K. Watanabe, Phys. Rev. B **85**, 245420 (2012).
[63] C. R. Ferreira, S. H. Pulcinelli, L. Scolfaro, and P. D. Borges, ACS Omega **4**, 14369 (2019).
[64] J. Heyd, G. E. Scuseria, and M. Ernzerhof, J. Chem. Phys. **118**, 8207 (2003).